

The effect of stress-level on the response of a model monopile to cyclic lateral loading in sand

I. A. Richards, M. F. Bransby, B. W. Byrne, C. Gaudin, G. T. Houlsby

Date text written	19 th March 2020
Date text revised	21 st July 2020
Positions, affiliations and ORCID number of authors	I. A. Richards, Wood Thilsted, formerly Oxford University, ORCID 0000-0003-4241-6031 M. F. Bransby, Centre for Offshore Foundation Systems, Ocean Graduate School, The University of Western Australia, ORCID 0000-0001-8444-5995 B. W. Byrne, Oxford University, ORCID 0000-0002-9704-0767 C. Gaudin, Centre for Offshore Foundation Systems, Ocean Graduate School, The University of Western Australia, ORCID 0000-0002-6326-4551 G. T. Houlsby, Oxford University, ORCID 0000-0001-5807-8781
Contact details	I. A. Richards, Wood Thilsted, 1 st Floor, 91-94 Lower Marsh, London, SE1 7AB ionalicerichards@gmail.com / iar@woodthilsted.com
Number of words in main text	Approx. 6500
Number of figures	17
Number of tables	7

Abstract

Monopile foundations supporting offshore wind turbines are exposed to cyclic lateral loading which can cause accumulated pile displacement or rotation and evolution of the dynamic response. To inform the development of improved design methods, the monopile's response to cyclic lateral loading has been explored through small-scale physical modelling at 1g and in the centrifuge, and at large-scale in the field. There are advantages and disadvantages to each physical modelling technique, and the response may be most efficiently explored through a combination of modelling techniques. However, stress-level varies significantly between these techniques, and only centrifuge testing can simulate full-scale stress-levels. This paper explores the effect of stress-level on the response of a monopile foundation in dry sand to monotonic, unidirectional cyclic and multidirectional cyclic lateral loading with small-scale tests at 1g and in the centrifuge at 9g and 80g. With an identical set-up at each g-level, stress-level effects were isolated. Qualitatively, the responses are similar across the stress-levels, but some important quantitative differences are revealed. In particular, the rate of accumulation of pile displacement and the rate of change of secant stiffness under cyclic loading are found to reduce with increasing stress-level. The results highlight the need to simulate full-scale stress-levels to thoroughly understand foundation behaviour, but also demonstrate the qualitative insight that can be gained through 1g physical modelling. The data and trends presented in this paper provide input for the modelling of monopile responses at different stress-levels.

1 Nomenclature

A	Coefficient
B	Coefficient
C	Coefficient
d_{10}, d_{50}, d_{60}	Particle sizes
D	Pile outside diameter
D_R	Relative density
e	Void ratio
e_{MAX}	Maximum void ratio
e_{MIN}	Minimum void ratio
g	Acceleration due to gravity
G	Shear modulus
G_{MAX}	Maximum (small strain) shear modulus
G_s	Specific gravity
h	Pile loading eccentricity
H	Horizontal load
H_{AV}	Average load amplitude
H_{CYC}	Cyclic load amplitude
H_{MAX}	Maximum load (during cyclic loading)
H_{MIN}	Minimum load (during cyclic loading)
H_R	Reference load
I_R	Relative density index
k_s	Secant stiffness
k_{sl}	Secant stiffness on loading
k_{su}	Secant stiffness on unloading
k_{MAX}	Maximum (small displacement) stiffness
K_p	Passive earth pressure coefficient
L	Pile embedded length
m	Maximum point on cycle
n	g -level
N	Cycle number
p'	Mean effective stress
p_a	Atmospheric pressure
q_c	CPT cone resistance
Q	General variable
r	Reversal point on cycle
R	General variable
R_a	Roughness
R_n	Normalised roughness
t	Pile wall thickness
u	Displacement at load application point
Δu_M	Accumulated mean pile displacement
u_R	Reference displacement at load application point
α	General exponent
β	General exponent
γ	General exponent
γ'	Effective unit weight
γ'_{MIN}	Minimum effective unit weight
γ'_{MAX}	Maximum effective unit weight
ζ_b	Parameter characterising cyclic load amplitude
ζ_c	Parameter characterising cyclic load symmetry
η	Energy loss factor, General exponent
H	Hysteretic energy loss
ϕ'_p	Peak friction angle
ϕ'	Friction angle
σ'_{REF}	Reference effective stress-level
σ'_v	Vertical effective stress
σ'_{vo}	Initial vertical effective stress
ϕ'_{CS}	Critical state friction angle

1 Introduction

2 Monopiles are the principal foundation solution for offshore wind turbine (OWTs) in shallow to medium water
3 depths, and currently support 87% of OWTs in Europe (Wind Europe 2018). The response of these large-
4 diameter, hollow steel piles has been the subject of much recent research, as their geometry and load regime
5 differs from piles traditionally used for offshore oil and gas and onshore applications. Monopiles are subjected
6 to long-term multidirectional cyclic lateral loading, caused by a combination of wind, waves and current loads,
7 which has been shown in model tests to cause accumulated displacement or rotation of the foundation (*e.g.*
8 Li *et al.* (2010) to Truong *et al.* (2019)) and evolution of foundation stiffness (Leblanc *et al.*, 2010) and energy
9 dissipation (Abadie *et al.*, 2019). Accumulated rotation of the foundation is of particular concern as turbine
10 manufacturers specify strict rotation limits, while changes to foundation stiffness and energy dissipation
11 impact the dynamic response of the foundation and can enhance dynamic amplification of loads and increase
12 fatigue damage of the OWT structure (Bhattacharya 2014).

13 Given that monopiles may be up to 8 m in diameter (Sørensen *et al.*, 2017), with the latest designs being even
14 larger, it is neither practical nor economic to test monopiles at full-scale. However, physical modelling – at 1*g*,
15 in the centrifuge and at large (but reduced) scale in the field – has been used extensively to explore the
16 response of a monopile. Because cyclic tests often involve many thousands of cycles and need to be performed
17 under load-control, many cyclic campaigns have been performed at 1*g*, where full-scale stress-levels are not
18 simulated (*e.g.* Leblanc *et al.*, 2010; Nicolai & Ibsen, 2014; Arshad & O’Kelly, 2017). Some studies have explored
19 a monopile’s cyclic response in the centrifuge, simulating full-scale stress-levels, although the number of cycles
20 is limited (*e.g.* Li *et al.*, 2010; Klinkvort & Hededal, 2013; Truong *et al.*, 2019). Large-scale field testing has also
21 been performed to understand a monopile’s response (principally under monotonic loading) (Byrne *et al.*
22 2017). These tests provide valuable insight, with stress-level, grain size and installation method closer to that
23 at full-scale; however, large-scale tests are very costly and there is intrinsic residual uncertainty about the soil
24 conditions at each pile location.

25 Understanding a monopile’s response to realistic, multidirectional cyclic lateral loading is necessary for the
26 development of new design methods for the next generation of monopiles. Given the complexity of the
27 problem, it may be most efficiently explored through a combination of 1*g* tests, centrifuge tests and large-
28 scale field tests. However, stress-level varies significantly between these test types, and only centrifuge tests
29 are able to simulate the full-scale stress regime. Understanding the impact of stress-level on a monopile’s
30 cyclic response is therefore an important step in bringing together observations from various test types. Other
31 parameters such as grain size and installation method will also vary between these test types, but this work
32 focuses exclusively on stress-level.

The fundamental behaviour of sand depends on stress-level. For example, dilatancy and peak friction angle ϕ'_p increase approximately logarithmically with reducing stress-level (Bolton 1986), while the maximum shear modulus G_{MAX} increases as a power function of stress-level, with the exponent typically 0.5 (first reported for angular grains by Hardin (1965), with a more recent review by Oztoprak & Bolton (2013)). This stress-level dependent behaviour is reflected in the global foundation response, as observed by Ovesen (1975) for footings and Klinkvort (2012) for monotonically laterally loaded monopiles.

Few studies have explored the impact of stress-level on a monopile's response to cyclic lateral loading, despite the prevalence of 1g testing in this area. Rudolph *et al.* (2014a) and Rudolph *et al.* (2014b) report a decrease in accumulated displacement for centrifuge tests compared to 1g tests, while Nicolai *et al.* (2017) compare post-cyclic behaviour between 1g and centrifuge tests. However, the set-up and sand type differed between 1g and centrifuge tests in these studies, and so stress-level effects were not completely isolated.

This paper extends the work of Richards *et al.* (2019), and specifically addresses the important issue of stress-level, presenting the response of a monopile in dry sand to monotonic, unidirectional cyclic and multidirectional cyclic loading at three g-levels. Tests were performed in the 5 m radius beam centrifuge at The University of Western Australia (UWA) at 9g and 80g, with corresponding 1g tests performed on the laboratory floor. By varying the g-level, effective unit weight and stress-level were varied; and with an identical set-up at each g-level, stress-level effects were isolated from other phenomena.

Experimental set-up

Sample preparation

UWA superfine (SF) silica sand obtained from Sibelco Australia Limited was used for these tests, with properties summarised in Table 1. Samples were prepared by air pluviation into a square strongbox with base dimensions 996 × 996 mm, to a sample height of 376 mm. Three dense samples were prepared with an average unit weight $\gamma'_{av} = 17.00 \pm 0.20$ kN/m³ (average relative density $D_{R,av} = 87.4 \pm 5$ %). The samples were prepared dry to ensure fully-drained response during pile loading.

Table 1 – Properties of UWA SF sand (Chow *et al.* 2018)

Specific gravity	G_s	2.67	-
Particle size	d_{10}, d_{50}, d_{60}	0.12, 0.18, 0.19	mm
Minimum effective unit weight	γ'_{MIN}	14.69	kN/m ³
Maximum effective unit weight	γ'_{MAX}	17.40	kN/m ³
Maximum void ratio	e_{MAX}	0.78	-
Minimum void ratio	e_{MIN}	0.51	-
Critical state friction angle (triaxial testing)	ϕ'_{CS}	31.9	°

The piles were installed 'wished-in-place' during the sand raining process. While it is acknowledged that this installation method is not representative of full-scale monopile installation and that the pile installation

method can affect the lateral stiffness and bearing capacity (e.g. Klinkvort, 2012; Fan et al., 2019), this method avoids the introduction of complex stress-fields and local density changes through in-flight (or 1g) installation which may scale differently to the post-installation response investigated here.

Sand was first rained to the depth of the pile tip, before hanging the piles in position and raining around them. The sand surface was then vacuumed to achieve an average pile embedment $L_{av} = 167 \pm 3$ mm. Nine piles were installed per strongbox, with a minimum centre-to-centre spacing of $7.4D$. This layout was chosen to avoid significant boundary effects while maximising the number of tests per strongbox sample; the centre-to-centre spacing is in-line with previous studies (e.g. Leblanc et al., 2010; Abadie, 2015; Albiker et al., 2017).

Cone penetration tests (CPTs) were performed using a 7 mm diameter cone to characterise each soil sample. For sample S1, used for 1g testing, two CPTs were performed at each stage: (a) before testing and (b) after testing. For samples S2 and S3, used for testing at 9g and 80g respectively, one CPT was performed at each stage: (a) at 1g before spinning, (b) at ng before testing, (c) at ng after testing and (d) at 1g after spinning down. Figure 1 presents the CPT profiles measured at each g -level. At 1g, the S1 CPTs and the pre-spinning S2 and S3 CPTs show good consistency, in-line with the small variation in global unit weight measured across the samples. The consistency of the pre- and post-testing S2 and S3 CPTs also gives confidence in the homogeneity of the sample and insensitivity to repeated spin cycles associated with each monopile test. The post-spinning S2 and S3 CPTs show increased CPT resistance which may be attributed to overconsolidation effects given that these samples previously experienced higher stress levels (Gui et al., 1998; Roy et al., 2019). However, no monopile tests were performed on these overconsolidated samples.

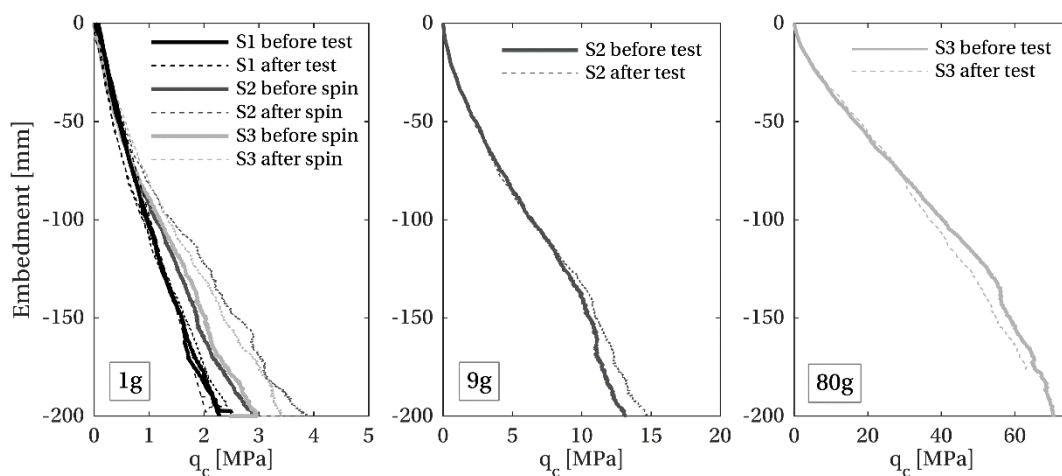


Figure 1 – CPT profiles

Model pile, loading and instrumentation

Tests were performed on sandblasted mild steel piles with properties summarised in Table 2. The small L/D ratio is representative of modern full-scale monopiles (Sørensen et al., 2017; Schroeder et al., 2015), while the

large h/D ratio is expected to be representative of operational loading conditions (Richards, 2019) and ensures a rotation-dominated response. The surface is classified as smooth on the basis of the normalised roughness R_n (e.g. Hu & Pu, 2004), in contrast to typically rough full-scale monopiles. However, roughness is likely to have only a small impact on the pile's lateral response (Klinkvort 2012). The pile has a closed-end which is appropriate given the wished-in-place installation method. Although full-scale monopiles are open-ended, the contribution of base shear and base moment is typically small (Burd *et al.*, 2020). The pile wall thickness is selected to ensure rigid behaviour at all three stress-levels; such rigid pile behaviour is expected to be representative for modern monopiles (e.g. Abadie, 2015).

Table 2 – Model pile properties

Outside diameter	D	42	mm
Target embedded length	L	168	mm
Length to diameter ratio	L/D	4	-
Wall thickness	t	3.2	mm
Eccentricity	h	424	mm
Eccentricity to diameter ratio	h/D	10	-
Mean surface roughness	R_a	3	μm
Normalised roughness	$R_n = R_a/d_{50}$	0.016	-

Figure 2 shows the loading and instrumentation apparatus, which was modified from that designed by Herduin (2019) for multidirectional loading of anchors. Actuators sit perpendicular to platform A and apply load to the pile via cables which travel around pulleys on platform C, and attach to inline load cells at the base of the pile stick-up. Pile displacement was measured with six string potentiometers. Three were positioned 253 mm above the load application point (on platform B) and three were positioned 30 mm above the load application point (on platform C). Each triplet of string potentiometers was arranged in a 120° star to attempt to eliminate the net load applied to the pile by these sensors, as each applies a tensile load of ~1 N in the direction of action. The pile stick-up allowed straightforward connection of the string potentiometers and load lines to the pile. The stick-up comprises an insert which is fixed inside the pile head and a threaded rod which the potentiometers and load lines were attached to.

The set-up shown in Figure 2 is for multidirectional loading, with three actuators and associated load lines positioned 120° apart. For unidirectional loading only two actuators were used, positioned 180° apart, to simplify the set-up. All cyclic tests were performed under load control with sinusoidal waveforms, while initial monotonic tests are performed under displacement control. Under load control, all load lines were kept in tension, with one or two lines typically holding constant load and one line applying cyclic loading.

To resolve pile position, vertical displacements were neglected and the planar position of the pile at the level of each triplet of string potentiometers was calculated. Under unidirectional loading, pile displacement was obtained directly from the string potentiometer aligned with the loading direction. Under multidirectional

1 loading, measurements from all three potentiometers were used, and to account for the measurement
 2 redundancy the error between actual and measured length was assumed to be equal for all three string
 3 potentiometers. Net loads were obtained directly under unidirectional loading, while under multidirectional
 4 loading they were resolved to account for the current pile position and load line angle.

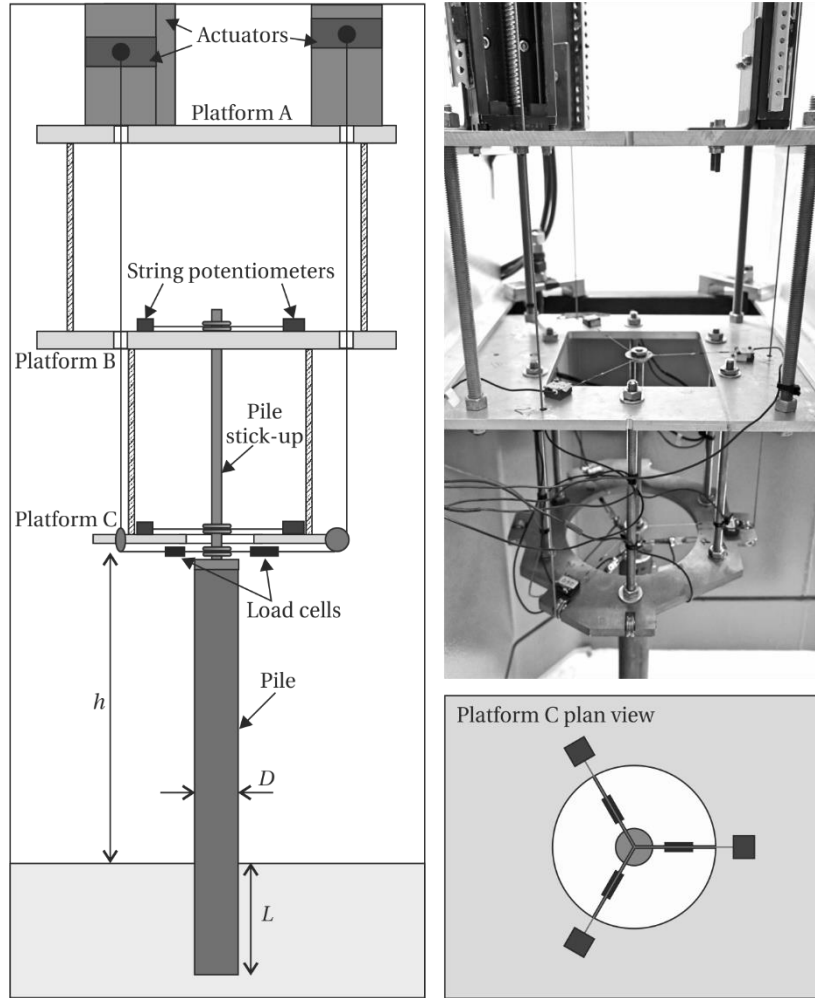


Figure 2 – Schematic (not to scale) and photograph of loading and pile measurement apparatus

Methodology

In this study, stress-level was controlled by varying the model g -level using the centrifuge. With the same set-up at each g -level, stress-level effects were isolated from other variables. The g -levels were chosen to vary logarithmically, in line with the expected logarithmic variation of dilatancy with stress-level.

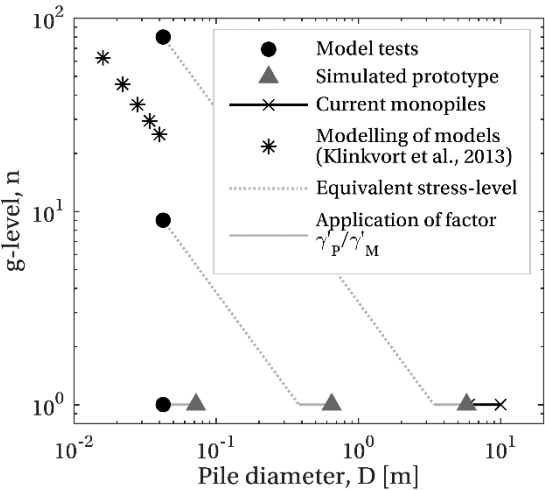
The vertical effective stress at 70% pile embedment was used as a reference effective stress-level ($\sigma'_{REF} = 0.7L\gamma'$) and as a proxy for the mean effective stress p' . For the model and sand sample ($\gamma'_M = 17 \text{ kN/m}^3$) used, Table 3 presents the reference effective stress-level and normalised effective stress-level (σ'_{REF}/p_a) corresponding to each g -level. Table 3 also presents the prototype monopile diameter D_P simulated at each g -level, assuming a dense, saturated sand at prototype-scale ($\gamma'_P = 10 \text{ kN/m}^3$). Figure 3 shows how the model

1 tests translate to prototype-scale. Although modern monopiles are even larger ($6 \text{ m} < D < 10 \text{ m}$) than that
 2 simulated by the 80g tests, the range of stress-levels is sufficiently large to observe relevant stress-level
 3 effects.

4 *Table 3 – Corresponding g-levels, normalised stress-levels and prototype pile diameters*

$g\text{-level}, n$	1	9	80
$\sigma'_{REF} \text{ [kPa]}$	2	18	162
$\frac{\sigma'_{REF}}{p_a}$	0.02	0.18	1.60
$D_P \text{ [m]}$	0.071	0.64	5.7

5
 6 ‘Modelling of models’ campaigns (*e.g.* Ovesen, 1975; Dewoolkar *et al.*, 1999; Klinkvort *et al.*, 2013) are more
 7 common than stress-level investigations, and involve tests at various g -levels and model sizes to simulate the
 8 same prototype response, to explore scale effects or verify centrifuge modelling techniques. An example
 9 modelling of models campaign performed by Klinkvort *et al.* (2013) is shown in Figure 3 for context.



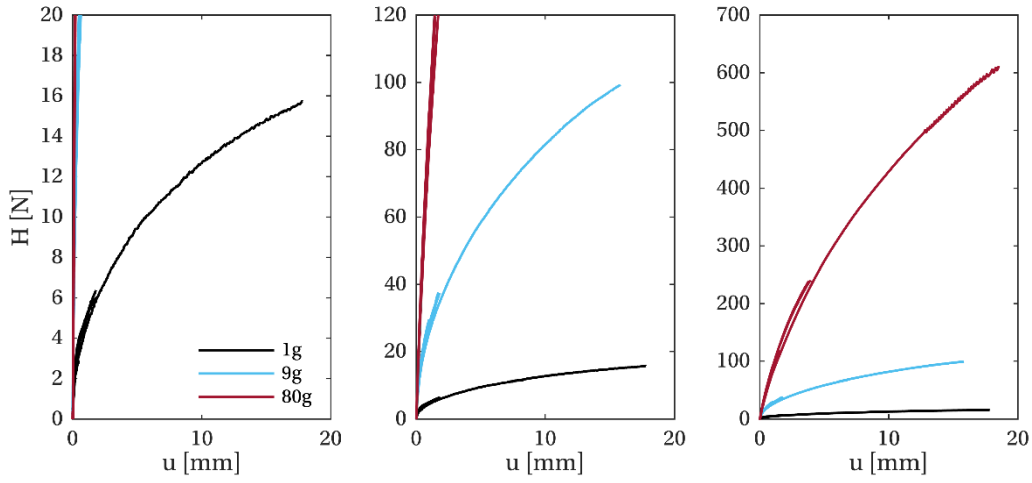
10
 11 *Figure 3 – Location of model tests at ng and equivalent prototypes at $1g$ relative to current full-scale monopiles*

12 Monotonic response

13 Figure 4 presents the response for the monotonic tests alongside the responses for the initial loading portion
 14 of the unidirectional cyclic tests. Figure 4 highlights the significant variation in response as the stress-level is
 15 varied, as well as the consistency of behaviour at each stress-level.

16 Data is presented in terms of applied horizontal load H and pile displacement at the load application point u
 17 (both at model-scale). The imperfectly rigid connection between the pile and pile stick-up introduces some
 18 error into the resolved pile rotation and prevents presentation of the response in terms of applied moment M

1 and pile rotation θ . However, conclusions on stress-level effects are not expected to be affected by the choice
 2 of either work-conjugate pair.



3
 4 *Figure 4 – Dimensional monotonic responses (data presented on three different y-axis scales to show responses at each stress-level)*

5 *Normalisation approaches*

6 Casting the monopile’s response in dimensionless form facilitates comparison of tests conducted across this
 7 large range of stress-levels, and can help provide insight into stress-level effects. Three different normalisation
 8 approaches are considered, following i) Klinkvort *et al.* (2013), ii) Klinkvort (2012) and iii) Leblanc *et al.* (2010),
 9 as summarised in Table 4.

10 *Table 4 – Comparison of normalisation approaches*

	i) Klinkvort <i>et al.</i> (2013)	ii) Klinkvort (2012)	iii) Leblanc <i>et al.</i> (2010) and Abadie (2015)
Load normalisation	$\frac{H}{D^3 \gamma'}$	$\frac{H}{K_p D^3 \gamma'}$ $K_p = \tan^2(45 + \phi'_p/2)$	$\frac{H}{L^2 D \gamma'}$
Displacement normalisation	$\frac{u}{D}$	$\frac{u}{D}$	$\frac{u}{D} \left(\frac{p_a}{L \gamma'} \right)^{\eta-1}$ $\eta = 0.5$

11
 12 Figure 5a shows the result of applying normalisation (i), which accounts for variation of γ' (but not for changes
 13 in stiffness or angle of friction) to the monotonic responses. This normalisation therefore highlights stress-
 14 level effects: the decrease in normalised initial stiffness and inferred normalised capacity with increasing
 15 stress-level is indicative of stress-dependent stiffness and dilatant behaviour.

16

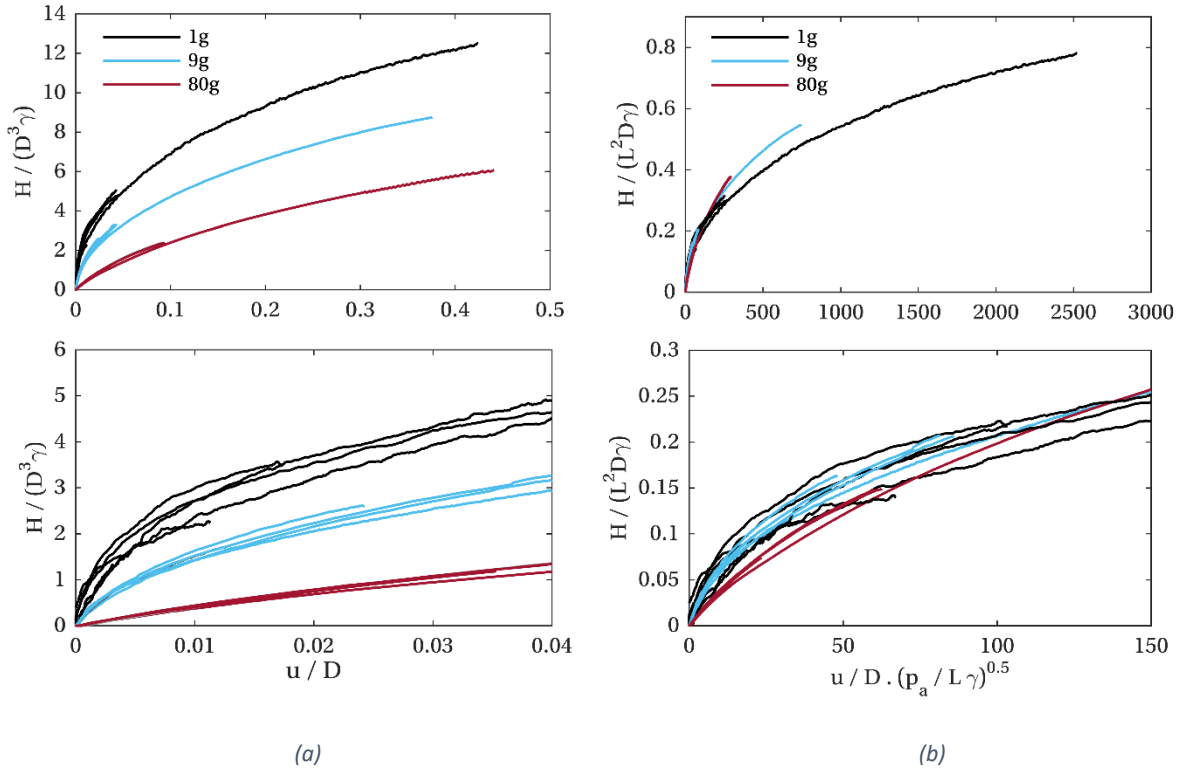


Figure 5 – Normalisation of monotonic responses (lower plots highlighting initial response) a) following Klinkvort et al. (2013); b) following Leblanc et al. (2010)

While exploring stress-level effects, Klinkvort (2012) proposed a further normalisation method (ii) which introduces Rankine's passive earth pressure coefficient K_p to attempt to account for stress-dependent changes in peak angle of friction ϕ'_p . Klinkvort (2012) used this normalisation to successfully collapse the response of a centrifuge model monopile at stress-levels from ~ 70 kPa to ~ 350 kPa, with ϕ'_p values obtained from complementary triaxial testing. Complementary triaxial tests are not available for this study, and moreover, obtaining definitive ϕ'_p values at stress-levels corresponding to the 1g tests (2 kPa) is likely to be very challenging. A number of relationships exist which allow ϕ'_p to be estimated for a given stress-level and relative density (Bolton, 1986; Bolton, 1987; Chakraborty & Salgado, 2010), but there is disagreement at low stress-levels. The relationship proposed by Bolton (1987), which limits dilatancy at low stress-levels, is employed in this work. This relationship is supported by the work of Tatsuoka (e.g. Tatsuoka et al., 1986) and the recent investigation into the behaviour of Leighton Buzzard sand by White (2020), which found that while the shear strength properties (e.g. ϕ'_p) tend to increase with decreasing effective confining stress, this effect becomes increasingly minor for confining stresses less than approximately 50 kN/m^2 . However, it is noted that other studies (Ponce & Bell, 1971; Quinteros et al., 2017) have presented conflicting results. Employing the relationship of Bolton (1987) to estimate ϕ'_p for normalisation (ii), K_p changes negligibly over the stress range of concern here, and the plot resembles Figure 5a.

In contrast to the approach of Klinkvort (2012), Leblanc *et al.* (2010) incorporates stress-dependent stiffness into normalisation (iii), but does not consider dilatancy (*i.e.* stress-level dependent changes in angle of friction). Stress-dependent stiffness is incorporated by assuming $G \propto p'^{\eta}$. The exponent is chosen as $\eta = 0.5$, which is generally accepted at small strains ($\gamma < 0.01\%$) *i.e.* $G_{MAX} \propto p'^{0.5}$ (*e.g.* Hardin, 1965). At larger strains $\eta \rightarrow 1$ (Oztoprak & Bolton 2013). Figure 5b shows the results of normalising with approach (iii). The normalisation successfully collapses the results towards a single curve, particularly at the small displacements that are relevant to the cyclic tests and which are expected to be controlled by small strain stiffness.

Together, the normalisations indicate the presence of stress-level dependent stiffness, and possibly stress-level dependent dilatant behaviour, although it is not possible to decouple these phenomena in this study. The normalisation approach of Leblanc *et al.* (2010) is adopted here for comparison of responses across stress-levels.

Maximum stiffness

The monopile's maximum tangential stiffness k_{MAX} is expected to vary with stress-level in the same way as the soil's maximum shear modulus G_{MAX} ; indeed, this assumption is incorporated into the normalisation approach of Leblanc *et al.* (2010).

The initial loading stiffness is the obvious choice for estimating k_{MAX} , but there is significant variability in this value, probably due to bedding-in effects associated with the wished-in-place installation method. Maximum tangential stiffness values obtained from the first unloading portion (available for all cyclic tests) are more consistent, and are therefore used here, although they may be affected by densification during initial (albeit small amplitude) loading.

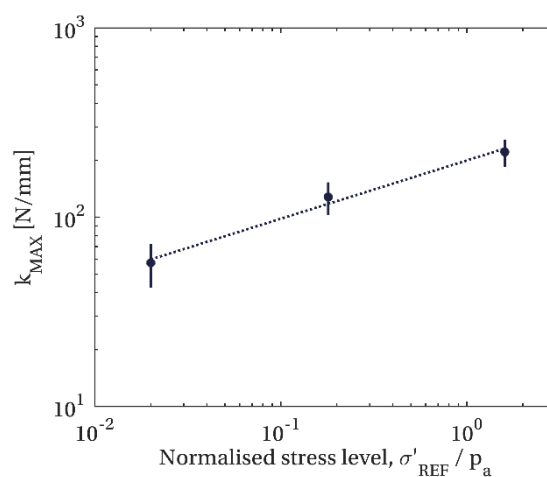


Figure 6 – Variation of first unloading (maximum) stiffness with stress-level (dotted line shows power function fit with $\eta = 0.31$)

Figure 6 presents the variation of k_{MAX} with stress-level. k_{MAX} is obtained by manual fitting to all relevant tests, and the range and mean values of k_{MAX} are indicated. A power function fits the variation of mean k_{MAX}

with stress-level well, as shown by the dotted line in Figure 6. However, the exponent obtained from least-squares fitting is $\eta = 0.31$, somewhat lower than the $\eta = 0.5$ for G_{MAX} that is implicit in the Leblanc *et al.*, (2010) normalisation. The cause of this discrepancy is unclear, but might be explained by experimental variability, the impact of stiffening during the initial loading portion, or three-dimensional effects when considering the monopile system. Using $\eta = 0.31$ in place of $\eta = 0.5$ in normalisation (iii) produces a poorer result.

Cyclic definitions

Loading

Constant amplitude cyclic loading can be characterised by two parameters (Leblanc *et al.* 2010):

$$\text{Equation 1} \quad \zeta_b = \frac{H_{MAX}}{H_R}$$

$$\text{Equation 2} \quad \zeta_c = \frac{H_{MIN}}{H_{MAX}}$$

Where H_{MAX} and H_{MIN} are the maximum and minimum loads applied in each cycle respectively. ζ_c characterises the load symmetry ($\zeta_c = 0$ for one-way loading, $\zeta_c = -1$ for symmetric two-way loading, $\zeta_c = 1$ for constant loading), while ζ_b and ζ_c together describe the load amplitude, relative to an arbitrary reference load H_R . Here, H_R is defined at a reference pile displacement value $u_R = 17.8$ mm at the load application point. This reference displacement approximately corresponds to 2° pile rotation ($\theta_R = 2^\circ$) and $0.1D$ pile displacement at the mudline, which may represent an ultimate failure criteria; similar reference values have been used in studies by Abadie *et al.* (2015) and Arshad and O'Kelly (2017). Table 5 summarises the monopile's reference load values at each g -level, obtained from initial monotonic tests.

The average load amplitude $H_{AV} = (H_{MAX} + H_{MIN})/2$ and cyclic load amplitude $H_{CYC} = (H_{MAX} - H_{MIN})/2$ are also useful parameters that can be used to describe the cyclic response.

Table 5 – Reference load (H_R) values for the model monopile at each g -level

g -level, n	1	9	80
H_R [N]	15.7	99.5	597

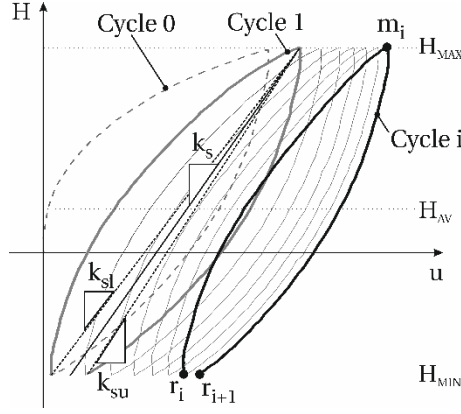


Figure 7 – Illustration of cycle, stiffness and energy loss factor definitions

Cyclic response

The monopile's cyclic response in dry sand is characterised in terms of permanent accumulation of displacement ('ratcheting'), evolution of secant stiffness and evolution of energy dissipation per cycle.

Ratcheting is interpreted in terms of accumulated mean displacement at the load application point (Δu_M), following the approach of Richards *et al.* (2019), but with displacement instead of rotation as the strain variable.

Secant stiffness k_s is defined at the centre of the cycle (as shown in Figure 7 for cycle 1) to minimise conflation of stiffness change with ratcheting. This stiffness is the inverse of the average of the loading and unloading flexibilities, and may be expressed in terms of the secant loading stiffness k_{sl} and secant unloading stiffness k_{su} , each indicated in Figure 7:

Equation 3

$$k_s = \frac{1}{\frac{1}{2} \left(\frac{1}{k_{sl}} + \frac{1}{k_{su}} \right)} = 2 \left(\frac{k_{sl} k_{su}}{k_{sl} + k_{su}} \right)$$

The energy dissipation is interpreted in terms of an energy loss factor η , proportional to the ratio of hysteretic energy loss H to maximum stored energy per cycle U_{max} (Inman 2014):

Equation 4

$$\eta = \frac{H}{2\pi U_{MAX}}$$

Where the maximum stored energy per cycle can be related to the secant stiffness as:

Equation 5

$$U_{MAX} = \frac{1}{8k_s} (H_{MAX} - H_{MIN})^2$$

For non-closing hysteresis loops (due to ratcheting) the hysteretic energy loss across a cycle i is defined as:

Equation 6

$$H_i = \int_{r_i}^{m_i} H(u) du + \int_{m_i}^{r_{i+1}} H(u) du$$

Where the reversal (r) and maximum (m) points are indicated in Figure 7. The energy loss factor becomes:

Equation 7

$$\eta = \frac{4k_s}{\pi(H_{MAX} - H_{MIN})^2} \left(\int_{r_i}^{m_i} H(u) du + \int_{m_i}^{r_{i+1}} H(u) du \right)$$

Unidirectional cyclic response

Test programme

Table 6 summarises the unidirectional cyclic tests conducted as part of this campaign. One-way ($\zeta_c = 0$) and two-way ($\zeta_c = -1$) tests were conducted, and the majority of tests involved 1000 initial loading cycles followed by a reload to $0.8H_R$ to explore the post-cyclic reloading response. The tests are characterised in terms of nominal and applied values of ζ_b and ζ_c . The nominal values are those demanded of the control system, while the applied loads are obtained from the in-line load measurements; the discrepancy is small and reduces with increasing load level, as the relative size of temperature effects and the load cell signal-to-noise ratio reduces.

Table 6 – Summary of unidirectional cyclic tests conducted

Test	g -level, n	ζ_b		ζ_c		No. of cycles, N	Reload
		Nominal	Applied	Nominal	Applied		
U.1.A	1	0.4	0.38–0.40	0	-0.03–0.02	1000	Yes
U.1.B	1	0.3	0.28–0.30	0	-0.06–0.05	770*	Yes
U.1.C	1	0.2	0.18–0.17	0	-0.06–0.06	1000	Yes
U.1.D	1	0.4	0.40–0.42	-1	-(0.97–0.89)	500**	No
U.9.A	9	0.4	0.39–0.40	0	-0.004–0.01	1000	Yes
U.9.B	9	0.3	0.29–0.30	0	-0.01–0.01	1000	Yes
U.9.C	9	0.2	0.19–0.20	0	-0.02–0.01	1000	Yes
U.9.D	9	0.4	0.39–0.40	-1	-(1.02–0.99)	1000	Yes
U.80.A	80	0.4	0.39–0.40	0	-0.006–0.02	1000	Yes
U.80.C	80	0.2	0.20–0.20	0	-0.002–0.004	1000	Yes
U.80.D	80	0.4	0.40–0.40	-1	-(1.01–0.99)	1000	Partial

*Final 230 cycles of test U.1.B excluded as they appear to be anomalous, probably due to temperature effects which were significant at $1g$.

**Only 500 cycles completed for test U.1.D, due to problems with load control.

Load-displacement response

Figure 8 presents the load-displacement ($H - u$) responses for the tests summarised in Table 6, alongside the corresponding monotonic responses ($M.n$). The full responses are shown for one-way tests U. n .A, U. n .B and U. n .C, while only the first five cycles of two-way tests U. n .D are shown to highlight the loop shape. The responses are normalised by the load and displacement reference values (H_R, u_R) to present data from all three stress-levels on comparable axes. The results show good repeatability at each stress-level and qualitatively similar behaviour across the three stress-levels, though it is clear that the responses become more linear with increasing stress-level. This variation in linearity is linked to stress-dependent stiffness and dilatant behaviour, as previously discussed, as well as the relative load amplitude. To better match the linearity

of the cyclic responses across the stress-levels, the reference pile displacement u_R – which determines H_R and therefore the cyclic amplitude ζ_b – may be adjusted with stress-level, perhaps employing the dimensionless framework of Leblanc *et al.* (2010). However, the variation in backbone linearity is a stress-level effect, and it is not clear whether it is appropriate to eliminate this effect by modifying u_R .

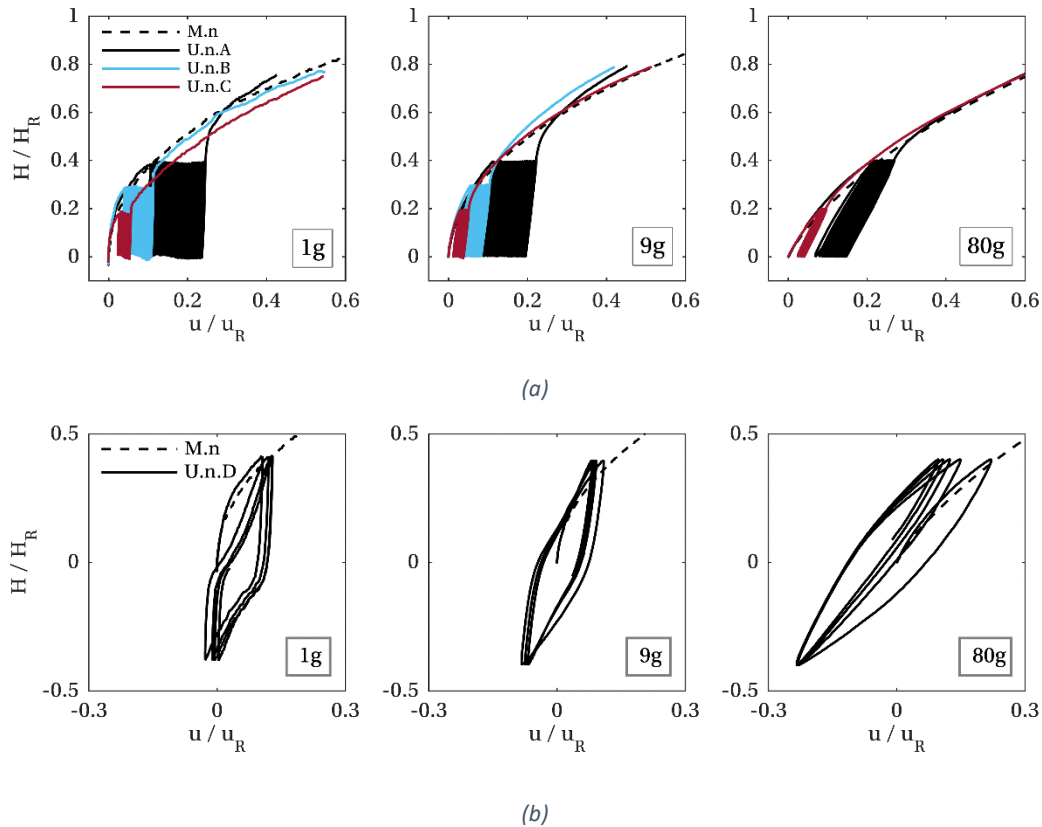


Figure 8 – Unidirectional cyclic loading load-displacement responses a) one-way; b) two-way (first 5 cycles)

Figure 8b also reveals evidence of gapping-like behaviour in tests U.n.D at 1g and to a lesser extent at 9g. The inflexion in the load-displacement response around zero load is indicative of a gapping-type response, as the tangent stiffness would reduce significantly while a pile traverses a gap. Similar load-displacement responses were recorded during field testing in both sand and clay as part of the PISA project, where gapping was also observed on site (Beuckelaers 2017). Gapping was not observed during these tests, but the set-up was not designed to record gap formation. A gap of only a fraction of a millimetre would be sufficient to account for the observed behaviour at 1g.

For these tests, the gapping-like behaviour reduces with increasing stress-level. Some ‘cohesion’ is necessary for gap formation, and so it is not generally expected in dry sand. However, the tendency for sand particles to move into a gap will reduce with reducing stress-level. At very low stress-levels, electrostatic effects or ambient moisture may then provide enough cohesion for gap formation. The wished-in-place installation will also lead to very low horizontal stresses adjacent to the pile, increasing the likelihood of gap formation.

Ratcheting response

Figure 9a presents evolution of normalised accumulated displacement ($\Delta u_M/u_R$) with cycle number (N) for the 1-way unidirectional cyclic tests; a power-law (Equation 8) is also fitted to each test response and shown dashed. Various studies have shown ratcheting to evolve approximately as a power-law with cycle number N (Leblanc *et al.*, 2010; Klinkvort, 2012; Abadie, 2015; Albiker *et al.*, 2017; Truong *et al.*, 2019), and a power law is also suitable here, at all stress-levels.

Equation 8

$$\Delta u_M/u_R = AN^\alpha$$

The power-law coefficient A has been found to vary with ζ_b and ζ_c (Leblanc *et al.*, 2010; Nicolai & Ibsen, 2014), while the power-law exponent α has often been reported as a constant within individual studies (Leblanc *et al.*, 2010; Nicolai & Ibsen, 2014; Albiker *et al.*, 2017). However, Truong *et al.* (2019) suggest that α varies with ζ_c and D_R . It should be noted that this paper investigates only a single value of ζ_c and D_R .

No dependence of A on stress-level is observed, although Figure 9b shows how A varies with ζ_b as a power law, in line with Abadie (2015):

Equation 9

$$A = \zeta_b^{0.34}$$

Conversely, no dependence of α on ζ_b is observed (in agreement with previous studies), but there is a trend for decreasing α with increasing stress-level, as shown in Figure 9c. To facilitate prediction of behaviour at other stress-levels, the ratcheting exponent α is presented in Figure 9c against normalised reference stress-level σ'_{REF}/p_a , rather than g -level.

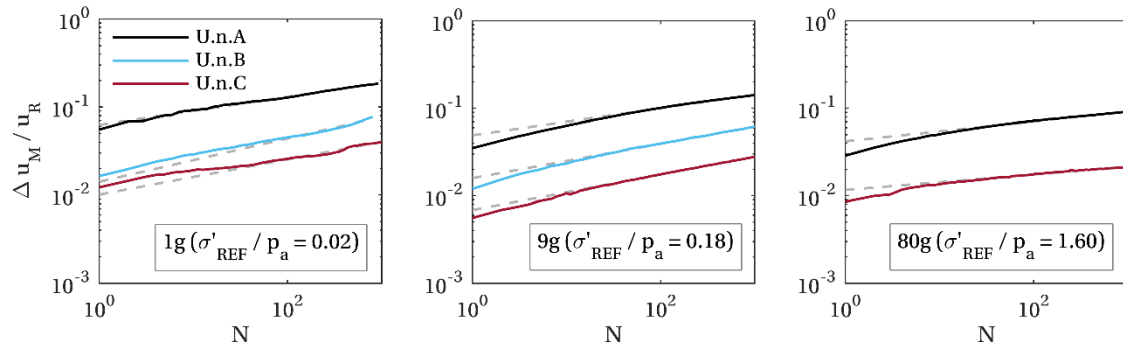
A logarithmic trend line is fitted to the data in Figure 9c to quantify the variation of α with stress-level, and shown dashed. The line is defined by:

Equation 10

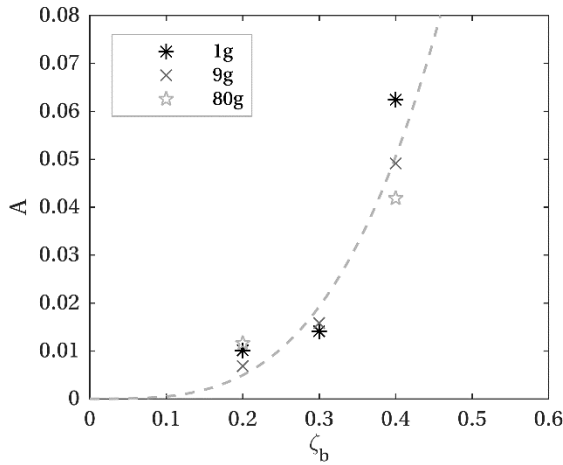
$$\alpha = 0.127 - 0.022 \ln\left(\frac{\sigma'_{REF}}{p_a}\right)$$

This trend line suggests that for a full size monopile in dense, saturated sand ($D = 8$ m, $\gamma' = 10$ kN/m³, $\sigma'_{REF}/p_a = 2.2$) the ratcheting exponent may be as low as 0.11, approximately half of the value in the 1g model tests.

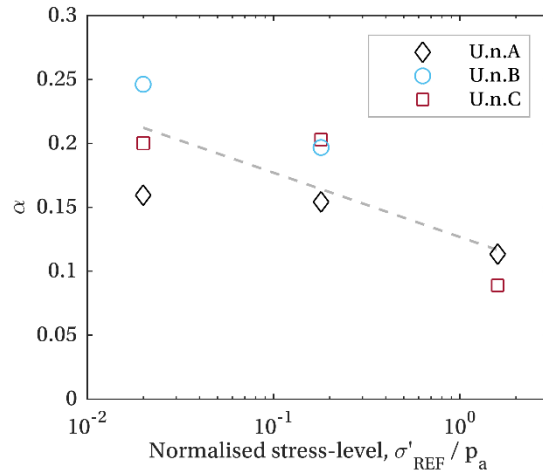
The value of α appears to vary with the chosen strain variable, and it is therefore difficult to compare α values from independent tests campaigns to build confidence in this conclusion on stress-dependency; for example, Albiker *et al.* (2017) find $\alpha = 0.23$ with pile rotation as the strain variable and $\alpha = 0.135$ with pile displacement (some distance above mudline) as the strain variable. However, the results presented here appear to be consistent with the increase in normalised pile displacement for 1g tests compared to centrifuge tests reported by Rudolph *et al.* (2014a) and Rudolph *et al.* (2014b).



(a)



(b)



(c)

Figure 9 – Unidirectional ratcheting response a) accumulation of displacement with cycle number N ; b) variation of ratcheting coefficient A with ζ_b ; c) variation of ratcheting exponent α with stress-level

Secant stiffness response

Figure 10a presents evolution of the monopile's secant stiffness k_s with cycle number for all unidirectional cyclic tests. Stiffness is normalised by the maximum stiffness k_{MAX} at each g -level, obtained from the first cycle unloading portion. An increase in secant stiffness with cycle number is observed for all tests, with k_s/k_{MAX} plateauing at high cycle number in all tests except U.1.D.

The initial normalised secant stiffness ($k_{s(N=1)}/k_{MAX}$) is plotted in Figure 10b. There is no strong dependence of general initial normalised secant stiffness values on stress-level, however, the spread of initial stiffness values decreases with increasing stress-level, consistent with the increasing linearity of the responses. At each g -level, the initial stiffness values generally decrease with cyclic amplitude H_{CYC} , as expected, given the non-linear load-displacement response.

Evolution of secant stiffness with cycle number has previously been described by logarithmic functions (Klinkvort & Hededal, 2013; Leblanc *et al.*, 2010; Abadie, 2015). Although a logarithmic function captures these data reasonably well, a power-law (Equation 11) fits equally well, and is preferred here for consistency of

1 interpretation with ratcheting. However, neither function captures the response particularly well for $N < 10$.
2 Power-law fits are shown dashed in Figure 10a.

Equation 11

$$k_s/k_{MAX,n} = BN^\beta$$

3 The impact of stress-level on the evolution of stiffness is assessed by plotting the power-law exponent (β)
4 against stress-level in Figure 10c. The exponents for tests U.1.D ($\beta = 0.304$) and U.9.D ($\beta = 0.110$) lie off this
5 plot, being considerably greater than the other exponents. These high values of β may be linked to the
6 gapping-like behaviour observed for these tests. If a gap is opening, the possibility of grain migration, and
7 therefore densification close to the pile, is increased.

8 A logarithmic trend line is fitted to the variation of β with stress-level, neglecting the two-way tests. The
9 dashed trend line in Figure 10c has equation:

Equation 12

$$\beta = 0.017 - 0.0076 \ln \left(\frac{\sigma'_{REF}}{p_a} \right)$$

10 This trend line suggests that for a full size monopile the 1-way stiffness exponent β may be as low as 0.011,
11 or 25% of the stiffness exponent value in the 1g model tests.

12 It should be noted that the power-law function for k_s (Equation 11) is not bounded as N approaches infinity.
13 However, given the small magnitude of β at the stress-levels of interest, reasonable values for secant stiffness
14 can be expected for all practical cycle numbers.

15

16

17

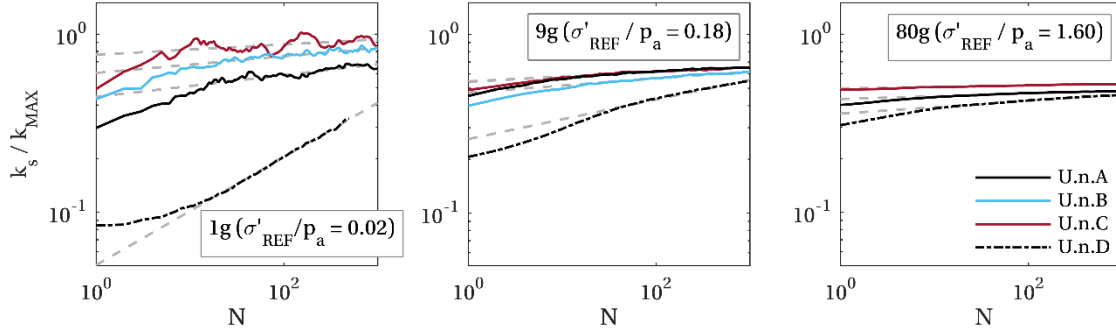
18

19

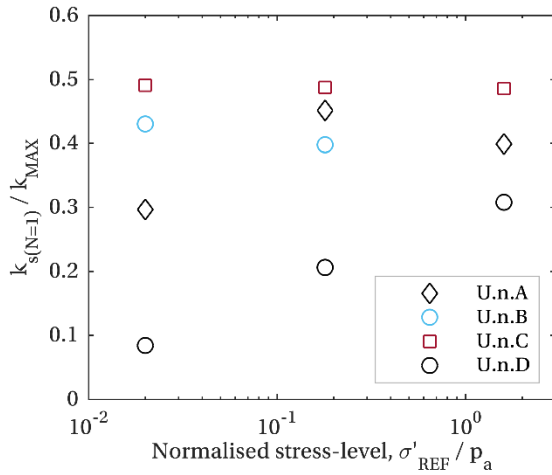
20

21

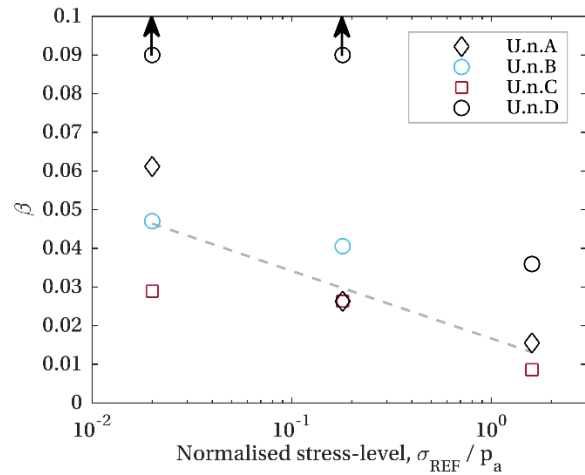
22



(a)



(b)



(c)

Figure 10 – Unidirectional secant stiffness response a) evolution of secant stiffness with cycle number N ; b) variation of initial secant stiffness with stress-level; c) variation of secant stiffness exponent β with stress-level

Energy loss factor response

Figure 11a shows the evolution of unidirectional energy loss factor with cycle number. Abadie (2015) also explored the evolution of an energy loss factor with cycle number and found a power-law adequately captured the evolution. A power-law (Equation 13) is also found to provide a good fit to the energy loss factor evolution here, at all stress-levels, and the resulting fits are shown dashed in Figure 11a.

Equation 13

$$\eta = CN^\gamma$$

As for ratcheting and stiffness evolution, the variation of the energy loss factor exponent γ with stress-level is plotted in Figure 11c. However, no dependence of γ on stress-level is observed. Instead, the initial energy loss factor $\eta_{N=1}$ is found to decrease with increasing stress-level, as shown in Figure 11b. Similar behaviour would be observed by plotting coefficient C against stress-level. The anomalously low value of initial energy loss factor for test U.1.D is linked to the significant gapping-like behaviour observed, which reduces the hysteretic energy loss H , compared to no gapping.

1 A logarithmic function is fitted to the variation of initial energy loss factor $\eta_{N=1}$ with stress-level. The following
 2 equation defines this trend line:

Equation 14

$$\eta_{N=1} = 0.228 - 0.134 \ln\left(\frac{\sigma'_{REF}}{p_a}\right)$$

3 This trend line suggests an initial energy loss factor of around 0.12 for an equivalent full size monopile, which
 4 is 16% of the value in the 1g model tests.

5 As for secant stiffness, the power-law function for η (Equation 13) is not bounded as N approaches infinity.
 6 However, given the small magnitude of γ at the stress-levels of interest, reasonable (non-negligible) values of
 7 energy loss factor are expected for all practical cycle numbers.

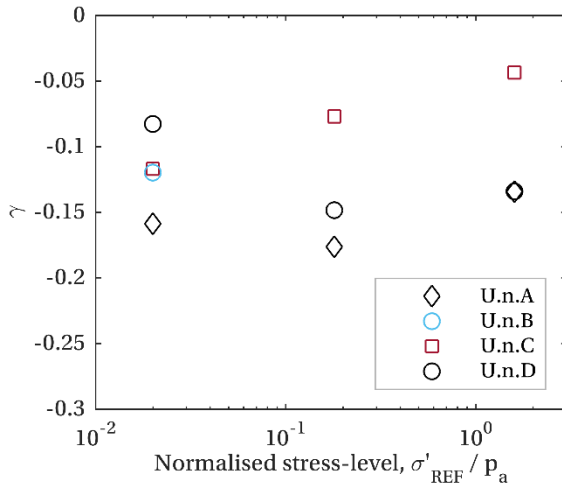
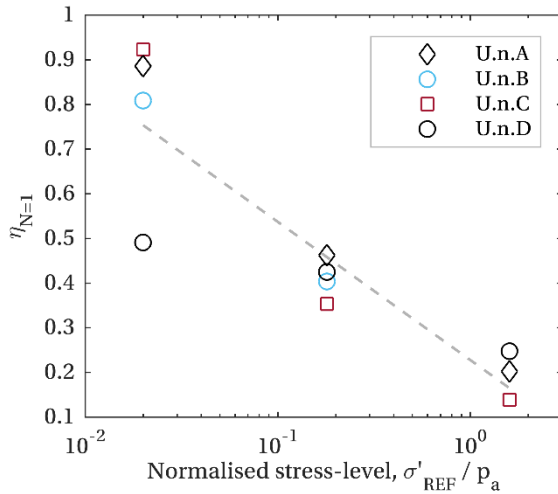
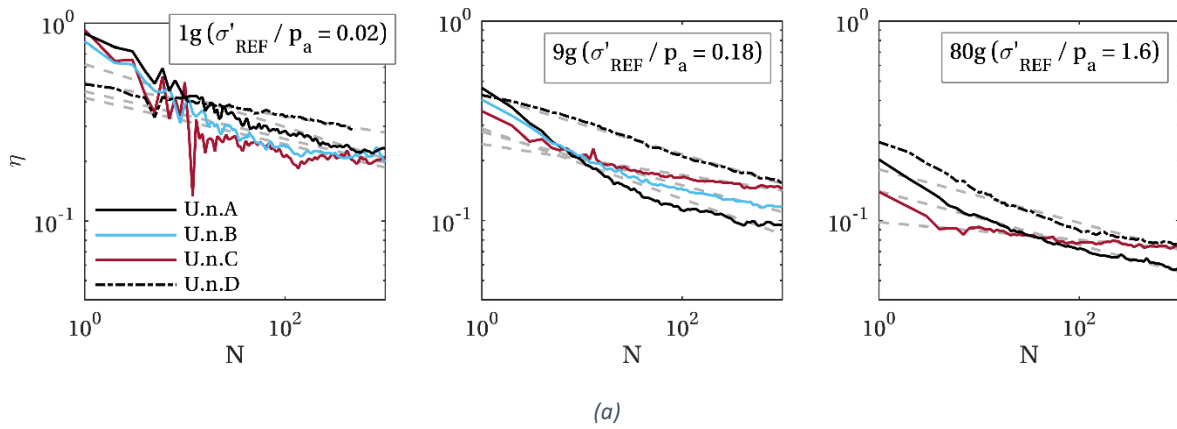


Figure 11 – Unidirectional energy loss factor a) evolution of energy loss factor with cycle number N ; b) variation of initial energy loss factor with stress-level; c) variation of energy loss factor exponent γ with stress-level

Reloading response

Post-cyclic reloading was performed after 1000 loading cycles for the majority of the unidirectional cyclic tests. Figure 8a shows how the reloading response tends to re-join the backbone curve following one-way cyclic loading at all stress-levels. It is understood that ratcheting and stiffening mechanisms act in competition, often

resulting in no significant net effect on the displacement response at large loads (Abadie *et al.*, 2019). The reloading response is also presented in Figure 12 with the displacement re-zeroed (from displacement at start of reload u_{r0}). This plot shows how the reloading response is significantly stiffer than the initial loading response for $H/H_R < \zeta_b$, consistent with the observed increase in secant stiffness with cycling. In general, when compared to the corresponding backbone curves, the reloading responses are qualitatively similar at all stress-levels.

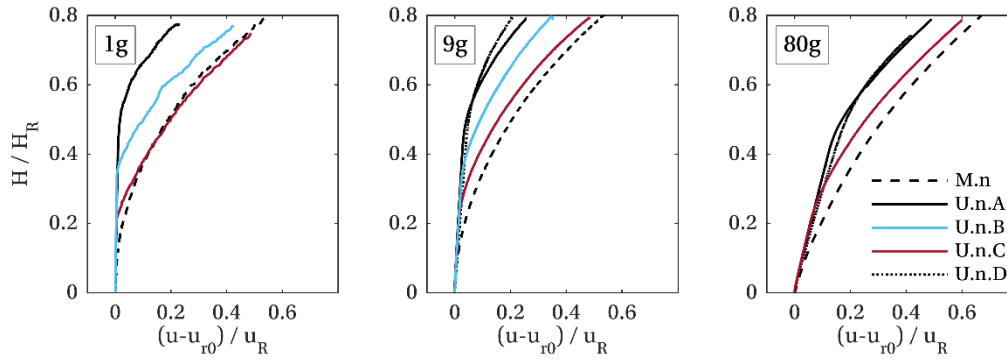


Figure 12 – Re-zeroed reloading response following unidirectional cyclic loading

Discussion

Qualitatively, the unidirectional cyclic response is similar across the three stress-levels investigated, with similar reloading responses and with power-law expressions approximately capturing the evolution of ratcheting, stiffness and energy loss factor at all stress-levels. Quantitatively, however, the results reveal some important stress-level effects.

The decrease of initial energy loss factor $\eta_{N=1}$ with stress-level can be directly linked to the linearity of the load-displacement response. The response linearity increases with stress-level for a given normalised load amplitude ζ_b , and is linked to stress-dependent stiffness and dilatant behaviour. However, the logarithmic decrease in ratcheting and stiffness exponent with stress-level (Figure 9c, Figure 10c) appears to be independent of load amplitude and therefore of linearity of the load-displacement response.

Cuéllar *et al.* (2012) and Nicolai (2017) explored the mechanism driving ratcheting and stiffening behaviour for cyclically loaded monopiles in sand. Cuéllar *et al.* (2012) used coloured sand grains at 1g and Nicolai (2017) used Particle Image Velocimetry in the centrifuge. Both authors observe local sand densification and convective particle movements during cyclic loading, and Cuéllar *et al.* (2012) identify 3D convective cells. Cui & Bhattacharya (2016) conducted DEM simulations to explore the same problem, and also observed convective particle movement and densification. Cui & Bhattacharya (2016) also suggest that the convective region is the shape of an inverted cone (also observed by Cuéllar (2011)) because increasing stress-level with depth imposes increasing constraint on particle movement.

The increase in the monopile's secant stiffness is probably caused by a local densification mechanism, while the ratcheting behaviour is probably caused by both a three-dimensional convective mechanism and any asymmetry in local densification. Given that both local densification and convective mechanisms require particle rearrangement, it is explicable that these mechanisms, and associated ratcheting and stiffening behaviour, will be affected by increasing stress-level, where – as highlighted by Cui & Bhattacharya (2016) – there is increasing constraint on particle rearrangement.

Multidirectional cyclic response

Test programme and loading definition

Table 7 summarises the multidirectional cyclic tests performed as part of this campaign. Two multidirectional tests were performed at each g -level: a T-shaped test and an L-shaped test. These tests explore the impact of cyclic load and load bias direction, and are intended to be compared to the one-way unidirectional tests at the same cyclic load amplitude H_{CYC} and average load amplitude H_{AV} .

Figure 13 shows the loading pattern for each test type: the selected unidirectional tests involve one-way cycling ($\zeta_c = 0$), T-shaped tests involve symmetric cycling ($\zeta_c = -1$) perpendicular to a constant load bias, and L-shaped tests involve one-way cycling ($\zeta_c = 0$) perpendicular to a constant load bias. Unidirectional, T-shaped and L-shaped tests therefore have average load biases in the II -direction, I -direction and at 45° to the axes respectively, following the axes in Figure 13. The T- and L-shaped tests may represent misaligned wave and wind loading on an OWT, where cyclic loading approximates wave loading and the load bias approximates the more slowly varying wind loading.

Table 7 – Summary of multidirectional cyclic tests conducted

Test	g - level, n	I-direction				II-direction				No. of cycles, N
		ζ_b		ζ_c		ζ_b		ζ_c		
		Nominal	Applied	Nominal	Applied	Nominal	Applied	Nominal	Applied	
M.1.T	1	0.35	0.37–0.39	1	0.80–1.05	0.2	0.19–0.22	-1	-(1.20–0.80)	250*
M.1.L	1	0.35	0.36–0.39	1	0.98–1.08	0.4	0.37–0.38	0	-(0.07–0.00)	153*
M.9.T	9	0.2	0.20–0.23	1	0.95–0.99	0.2	0.19–0.20	-1	-(1.03–0.99)	1000
M.9.L	9	0.2	0.21–0.24	1	0.93–0.97	0.4	0.39–0.38	0	-(0.06–0.00)	1000
M.80.T	80	0.2	0.20–0.22	1	0.95–1.00	0.2	0.20–0.20	-1	-(1.00–0.95)	1000
M.80.L	80	0.2	0.20–0.22	1	0.95–1.00	0.4	0.39–0.39	0	-(0.02–0.00)	1000

* Fewer than 1000 cycles completed for these tests, due to load control problem.

Table 7 characterises the tests in terms of nominal and applied values of ζ_b and ζ_c . The nominal values are those demanded of the control system during testing, without considering load adjustment due to pile movement. The applied values are resolved from the load cell measurements post-test, accounting for the current pile position and load line angle. The multidirectional tests at 9g and 80g correspond to unidirectional

tests U.n.A, conducted at the same cyclic load amplitude H_{CYC} and average load amplitude H_{AV} . The multidirectional 1g tests have a nominal load bias in the I -direction 75% larger than U.1.A, and comparisons at 1g should therefore be made with caution.

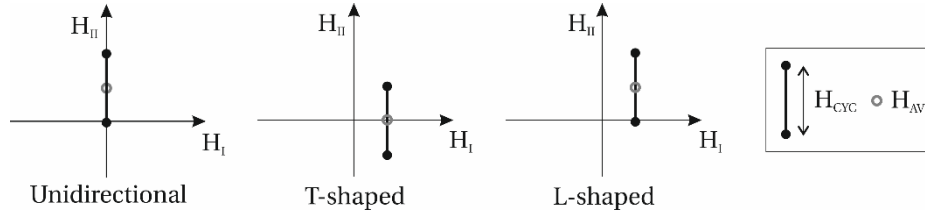


Figure 13 – Schematic demonstrating multidirectional loading

Displacement and ratcheting response

Figure 14 presents the displacement response for the multidirectional tests summarised in Table 7, alongside the corresponding unidirectional tests. The displacements at cycles 1, 10, 100, (1000) are marked. Figure 14 shows how the monopile moves broadly in the direction of the load bias at all stress-levels, though there is some deviation in M.9.T and M.80.T. Figure 14 also highlights the increase in amplitude of cyclic displacement with stress-level, which is in-line with the changing linearity of the load-displacement response with stress-level.

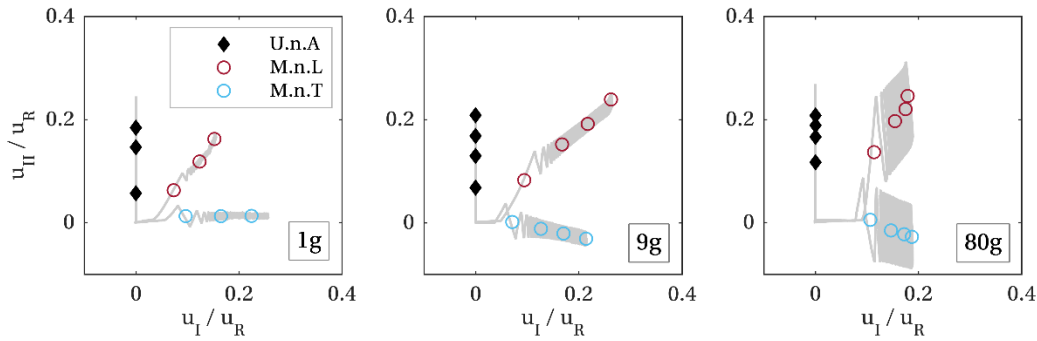


Figure 14 – Displacement response for multidirectional tests (markers indicate displacement at cycle 1, 10, 100, (1000))

Figure 15a presents the accumulated displacement response for the multidirectional tests alongside the corresponding unidirectional tests. Multidirectional behaviour is presented in terms of orthogonal I - and II -direction components. For the T-shaped tests significant ratcheting only occurs, and is only reported, in the I -direction. For the L-shaped tests ratcheting is reported in both the I - and II -directions. A power-law (Equation 8) is fitted to the evolution of $\Delta u_M/u_R$ with cycle number and shown dashed in Figure 15a. The power-law generally captures the evolution of ratcheting well for $N > 10$, but tends to over-predict ratcheting for $N < 10$ for the T-shaped test. The response of test M.80.L(I), particularly for $N > 100$, may be anomalous.

Figure 15b presents the variation of ratcheting coefficient A with test type and stress-level. No clear dependence of A on either test type or stress-level is observed. The ratcheting exponent α is plotted against stress-level in Figure 15c, accompanied by the dashed trend line obtained for the unidirectional tests (Equation 10). This trend line also fits the multidirectional data well. In general, Figure 15 shows no clear dependency of ratcheting behaviour on test type (at least for $N > 10$).

The greater scatter in Figure 15b and Figure 15c for the 1g tests is explained by the inconsistency in applied load bias.

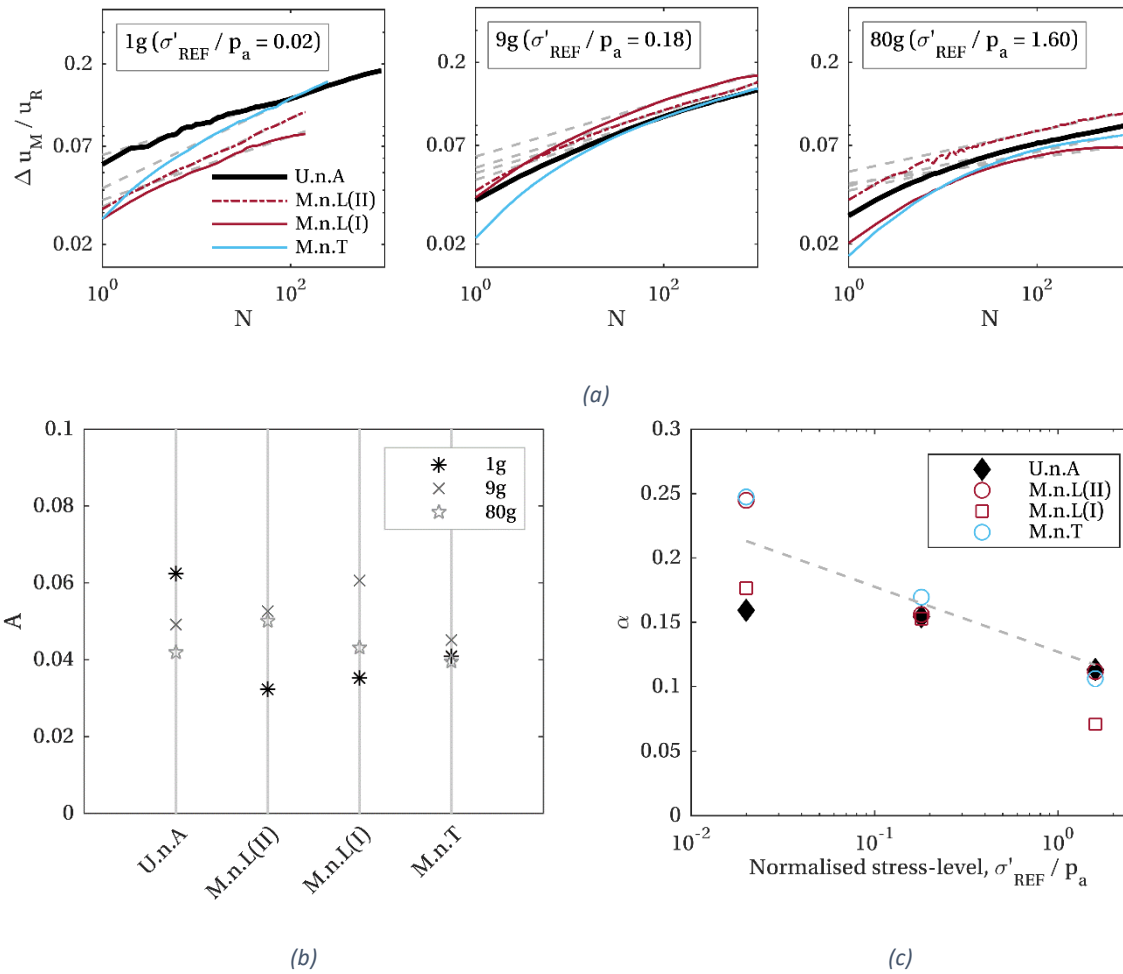
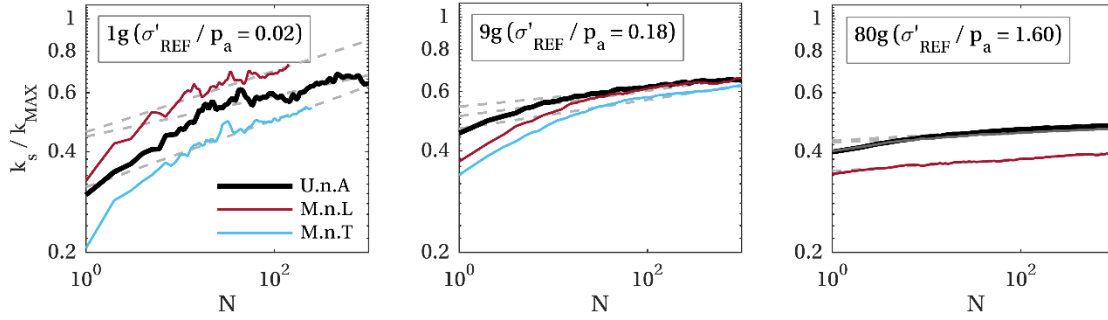


Figure 15 – Multidirectional ratcheting response a) accumulation of displacement with cycle number N ; b) variation of ratcheting coefficient A with multidirectional loading type; c) variation of ratcheting exponent α with stress-level

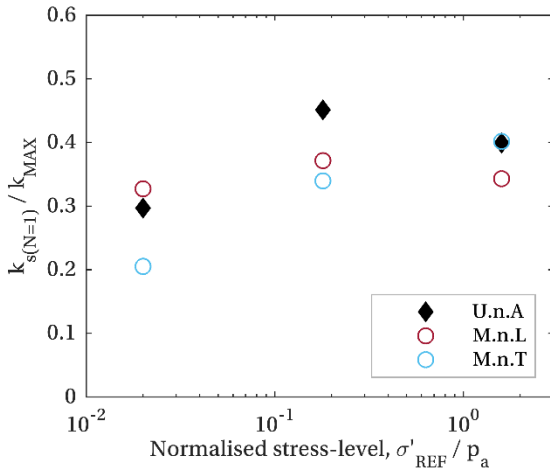
Secant stiffness response

Figure 16a presents the evolution of secant stiffness for the multidirectional tests and corresponding unidirectional cyclic tests. For multidirectional loading, evolution of secant stiffness is only relevant in the direction of cycling. For $N > 10$, the response is well described with a power law (Equation 11), which is fitted and shown dashed in Figure 16a.

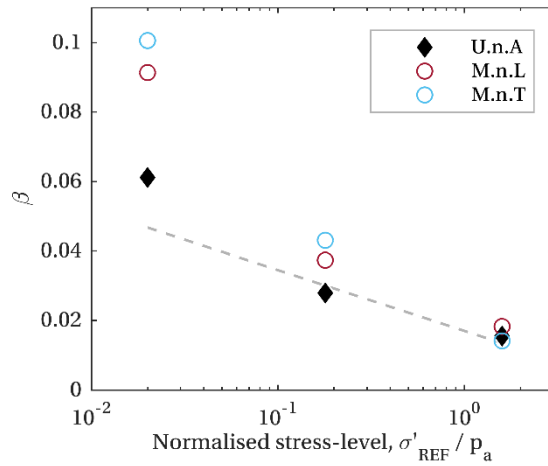
1 The variation of initial normalised secant stiffness ($k_{s(N=1)}/k_{MAX}$) is shown in Figure 16b. As for the
 2 unidirectional tests, there is no dependence on stress-level; there is also no dependence on test type. The
 3 variation in stiffness exponent β is plotted in Figure 16c, with the trend line obtained for unidirectional loading
 4 (Equation 12) shown dashed. The values of β for the multidirectional tests at 1g depart from the trend line
 5 (although this may be related to the inconsistency in applied load bias), while the multidirectional tests at 9g
 6 and 80g are aligned with the unidirectional trend.



(a)



(b)

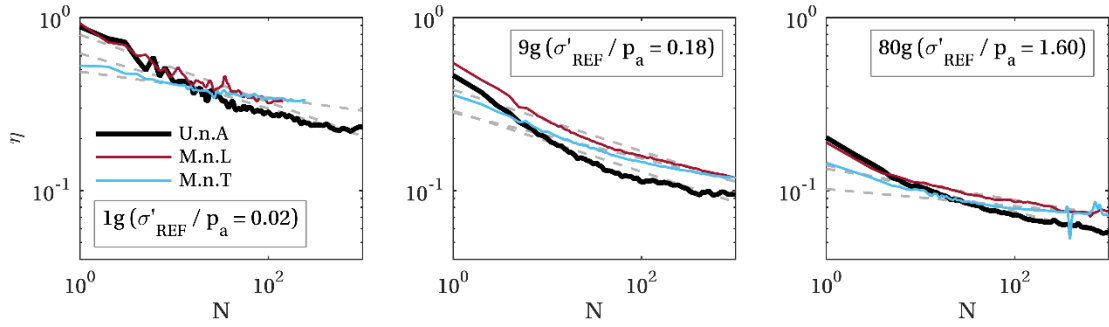


(c)

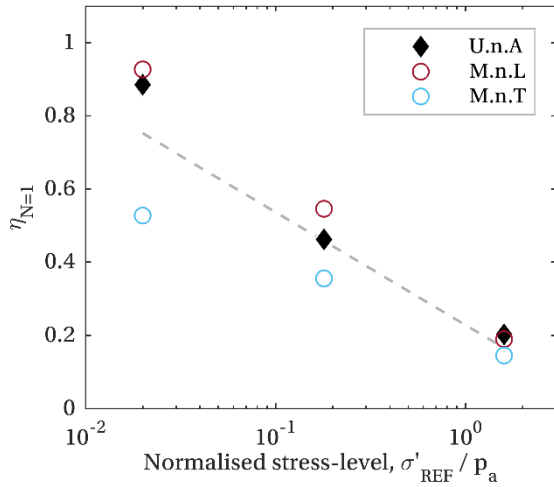
Figure 16 – Multidirectional secant stiffness response a) evolution of secant stiffness with cycle number N ; b) variation of initial secant stiffness with stress-level; c) variation of secant stiffness exponent β with stress-level

Energy loss factor response

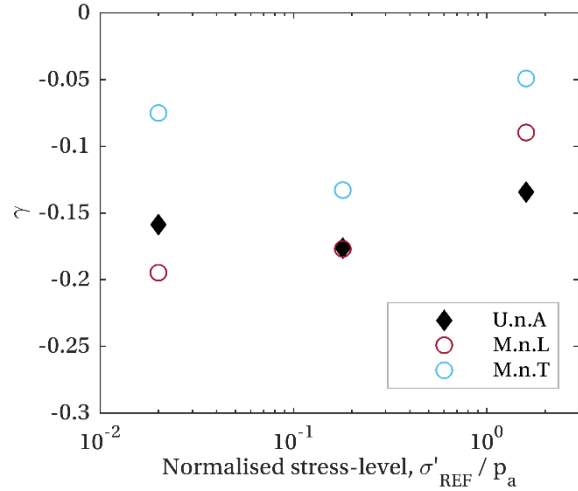
14 The evolution of energy loss factor with cycle number is shown in Figure 17a, with a power law (Equation 13)
 15 fitted and shown dashed. The multidirectional behaviour is consistent with that observed for the unidirectional
 16 tests: there is no clear dependence of the energy loss factor exponent on stress-level (Figure 17c), but the
 17 initial energy loss factor $\eta_{N=1}$ decreases logarithmically with stress-level (Figure 17b). The trend line obtained
 18 for unidirectional loading (Equation 14) also fits this data well, as shown by the dashed line in Figure 17b. There
 19 is no clear variation in initial energy loss factor or exponent with test type.



(a)



(b)



(c)

Figure 17 – Multidirectional energy loss factor a) evolution of energy loss factor with cycle number N ; b) variation of initial energy loss factor with stress-level; c) variation of energy loss factor exponent γ with stress-level

Discussion

In general, the stress-level effects observed in the unidirectional tests are also observed in the multidirectional tests. The trend lines obtained from the unidirectional results for variation of ratcheting exponent, stiffness exponent and initial energy loss factor with stress-level are also appropriate for the multidirectional results.

For $N < 10$, the T-shaped tests exhibit less accumulated displacement than the corresponding L-shaped and unidirectional tests. However, in general there is little variation in magnitude and evolution of ratcheting, stiffness and energy loss factor with test type, at all stress-levels. This implies that, for a given mean load H_{AV} and cyclic load amplitude H_{CYC} , the direction of cyclic loading relative to the mean load has an insignificant impact on the cyclic response. Ratcheting is also seen to occur in the direction of the mean load at all stress-levels, regardless of the cyclic loading direction, in agreement with Richards *et al.* (2019). These observations have important modelling implications, and suggest that misaligned wind and wave loading may be as damaging as aligned wind and wave loading.

1 Conclusions

2 Lateral monotonic, unidirectional cyclic and multidirectional cyclic loading tests have been performed on a
3 model monopile in dry, dense sand at three different g -levels, to investigate stress-level effects.
4 Stress-level effects were isolated experimentally by using the same experimental set-up at each g -level.

5 The monotonic responses exhibit stress-level effects which appear to be mostly explained by stress-dependent
6 stiffness, with some contribution from stress-dependent dilatancy, although decoupling these phenomena is
7 difficult. The monotonic responses support the use of the normalisation approach proposed by Leblanc *et al.*
8 (2010), particularly at small displacements. However, a lower exponent than that implied in the Leblanc *et al.*
9 (2010) normalisation was obtained when exploring the stress-dependency of maximum (small-displacement)
10 foundation stiffness.

11 Qualitatively, the cyclic responses are similar across the stress-levels, with similar post-cyclic reloading
12 behaviour and with power-law expressions approximately capturing the evolution of ratcheting, stiffness and
13 energy loss factor with cycle number. Quantitatively, however, the results reveal some important stress-level
14 effects.

15 The ratcheting and stiffness exponents, which control the rate of change of these parameters with cycle
16 number, both decrease logarithmically with increasing stress-level. The trends suggest that at full-scale the
17 ratcheting exponent may be around half of the value obtained in $1g$ model tests, while the stiffness exponent
18 is projected to reduce to 25% of the $1g$ model test value at full-scale. This behaviour is explained by the
19 increase in confinement with stress-level, which inhibits the particle movements which are thought to cause
20 ratcheting and stiffness change with cycling.

21 In this study, the model reference pile displacement u_R – which determines the reference load amplitude H_R
22 – was maintained constant (in absolute terms) with stress-level. As a result, the linearity of the monotonic and
23 cyclic responses (at a given ζ_b) increases with increasing stress-level; correspondingly, the initial energy loss
24 factors reduce with increasing stress-level. Future studies into the effect of stress-level on the cyclic response
25 might change or minimise the effect of the backbone linearity by setting the reference pile displacement, u_R ,
26 in a different way (*e.g.* by employing a constant dimensionless value).

27 The multidirectional tests exhibit stress-level effects consistent with the unidirectional tests, and provide
28 insight into the impact of cyclic load direction. For a given mean load and cyclic load amplitude, the cyclic
29 direction has no significant impact on the cyclic response, while ratcheting occurs in the direction of the mean
30 load.

31 This test campaign provides new insight into the impact of stress-level on the response of a monopile, with
32 the monotonic response and evolution of ratcheting and stiffness exhibiting significant stress-level

dependency. The stress-level effects highlight the need to simulate full-scale stress-levels to understand foundation behaviour thoroughly, while the qualitative similarities in response demonstrate the insight that can be gained from 1g testing. The trends presented in this paper can help compare monopile behaviour observed at different stress-levels, using different physical modelling approaches, to inform better the development of new design methods for the next generation of monopile foundations.

Data Availability Statement

Data that support the findings of this study (pile load displacement responses) are available from the corresponding author upon reasonable request.

Acknowledgements

Centrifuge tests were undertaken with the support of the technical team at the National Geotechnical Centrifuge Facilities at UWA, whose contribution is gratefully acknowledged. We would also like to thank Manuel Herduin for assistance when using a modified version of his apparatus. The second author is supported as the Fugro Chair in Geotechnics.

This work was supported by grant EP/L016303/1 for Cranfield University, the University of Oxford and Strathclyde University, Centre for Doctoral Training in Renewable Energy Marine Structures (REMS, <http://www.rems-cdt.ac.uk/>) from the UK Engineering and Physical Sciences Research Council (EPSRC).

1 References

- 2 Abadie, C.N., 2015. Cyclic lateral loading of monopile foundations in cohesionless soils, DPhil thesis, University
3 of Oxford.
- 4 Abadie, C.N., Byrne, B.W. & Houlsby, G.T., 2019. Rigid pile response to cyclic lateral loading: laboratory tests.
5 *Géotechnique*, 69(10).
- 6 Albiker, J., Achmus, M., Frick, D. & Flindt, F., 2017. 1g Model Tests on the Displacement Accumulation of Large-
7 Diameter Piles Under Cyclic Lateral Loading. *Geotechnical Testing Journal*, 40(2), 173–184.
- 8 Arshad, M. & O’Kelly, B., 2017. Model Studies on Monopile Behavior under Long-Term Repeated Lateral
9 Loading. *International Journal of Geomechanics*, 17(1).
- 10 Beuckelaers, W.J.A.P., 2017. Numerical Modelling of Laterally Loaded Piles for Offshore Wind Turbines, DPhil
11 thesis, University of Oxford.
- 12 Bhattacharya, S., 2014. Challenges in Design of Foundations for Offshore Wind Turbines. *Engineering &*
13 *Technology Reference, IET*.
- 14 Bolton, M.D., 1987. Reply to discussion on: The strength and dilatancy of sands, Bolton (1986). *Géotechnique*,
15 37(2), 219–226.
- 16 Bolton, M.D., 1986. The strength and dilatancy of sands. *Géotechnique*, 36(1), 65–78.
- 17 Burd, H.J., Taborda, D.M.G., Zdravković, L., Abadie, C.N., Byrne, B.W., Houlsby, G.T., Gavin, K., Igoe, D., Jardine,
18 R.J., Martin, C.M., McAdam, R.A., Pedro, A.M.G. and Potts, D.M. (2020). PISA Design Model for Monopiles for
19 Offshore Wind Turbines: Application to a Marine Sand, *Géotechnique*, ahead of print,
20 doi:10.1680/jgeot.18.p.277
- 21 Byrne, B.W. et al., 2017. PISA: New design method for offshore wind turbine monopiles. In Proceedings of the
22 *8th International Conference on Offshore Site Investigation and Geotechnics (SUT)*, 142-161. London, UK.
- 23 Chakraborty, T. & Salgado, R., 2010. Dilatancy and Shear Strength of Sand at Low Confining Pressures. *Journal*
24 *of Geotechnical and Geoenvironmental Engineering*, 136(1), 527–532.
- 25 Chow, S., Roy, A., Herduin, M., Heins, E., King, L., Bienen, B., O’Loughlin, C., Gaudin, C., Cassidy, M., 2018.
26 Characterisation of UWA superfine silica sand, Internal report, Oceans Graduate School, University of Western
27 Australia.
- 28 Cuéllar, P., Georgi, S., Baeßler, M., Rücker, W., 2012. On the quasi-static granular convective flow and sand
29 densification around pile foundations under cyclic lateral loading. *Granular Matter*, 14(1), 11–25.

1 Cuéllar, V.P., 2011. Pile Foundations for Offshore Wind Turbines : Numerical and Experimental Investigations
2 on the Behaviour under Short-Term and Long-Term Cyclic Loading. PhD Thesis, Technischen Universität Berlin.

3 Cui, L. & Bhattacharya, S., 2016. Soil-monopile interactions for offshore wind turbines. *Proceedings of the*
4 *Institution of Civil Engineers - Engineering and Computational Mechanics*, 169(4), 171–182.

5 Dewoolkar, M.M., Pak, R.Y.S. & Ko, H.-Y., 1999. Centrifuge modelling of models of seismic effects on saturated
6 earth structures. *Géotechnique*, 49(2), pp.247–266.

7 Fan, S., Bienen, B. & Randolph, M.F., 2019. Centrifuge study on effect of installation method on lateral
8 response of monopiles in sand. *International Journal of Physical Modelling in Geotechnics*, 2019, pp.1-13.

9 Gui, M.W., Bolton, M.D., Garnier, J., Corte, J.F., Bagge, G., Laue, J., Renzi, R., 1998. Guidelines for cone
10 penetration tests in sand. *Proceedings of the International Conference on Centrifuge Modelling*, 155–160.

11 Hardin, B., 1965. Dynamic versus static shear modulus for dry sand. *Materials Research and Standards*, 5(5),
12 232-235.

13 Herduin, M., 2019. Multi-directional loading on shared anchors for offshore renewable energy: Definition and
14 preliminary investigation into soil behaviour and anchor performance. PhD Thesis, University of Western
15 Australia.

16 Inman, D.J., 2014. Engineering vibration, 4th ed., Pearson.

17 Klinkvort, R. & Hededal, O., 2013. Lateral response of monopile supporting an offshore wind turbine.
18 *Proceedings of the Institution of Civil Engineers - Geotechnical Engineering*, 166(2), 147–158.

19 Klinkvort, R., Springman, S. & Hededal, O., 2013. Scaling issues in centrifuge modelling of monopiles.
20 *International Journal of Physical Modelling in Geotechnics*, 13(2), 38–50.

21 Klinkvort, R.T., 2012. Centrifuge modelling of drained lateral pile-soil response. PhD Thesis, DTU.

22 Leblanc, C., Houlsby, G.T. & Byrne, B.W., 2010. Response of stiff piles in sand to long-term cyclic lateral loading.
23 *Géotechnique*, 60(2), 79–90.

24 Li, Z., Haigh, S.K. & Bolton, M.D., 2010. Centrifuge modelling of mono-pile under cyclic lateral loads. In
25 *Proceedings of the 7th International Conference on Physical Modelling in Geotechnics*. Zurich, 965–970.

26 Nicolai, G., 2017. Cyclic behaviour of laterally loaded monopiles in sand supporting offshore wind turbines.
27 PhD Thesis, Aalborg University.

28 Nicolai, G. et al., 2017. Quantifying the increase in lateral capacity of monopiles in sand due to cyclic loading.
29 *Géotechnique Letters*, 7(3), 1–8.

1 Nicolai, G. & Ibsen, L.B., 2014. Small-Scale Testing of Cyclic Laterally Loaded Monopiles in Dense Saturated
2 Sand. *Journal of Ocean and Wind Energy*, 1(4), 240–245.

3 Ovesen, N.K., 1975. Centrifugal testing applied to bearing capacity problems of footings on sand.
4 *Géotechnique*, 25(2), 394–401.

5 Oztoprak, S. & Bolton, M.D., 2013. Stiffness of sands through a laboratory test database. *Géotechnique*, 63(1),
6 54–70.

7 Ponce, V. M., & Bell, J. M. (1971). Shear strength of sand at extremely low pressures. *Journal of the Soil*
8 *Mechanics and Foundation Division*, ASCE, 97(SM4), 625–638.

9 Quinteros, V. S., Lunne, T., Dyvik, R., Krogh, L., Bøgelund-Pedersen, R., & Bøtke-Rasmussen, S. (2017).
10 Influence of Pre-Shearing on the Triaxial Drained Strength and Stiffness of a Marine North Sea Sand.
11 In Proceedings of the 8th International Conference on Offshore Site Investigation and Geotechnics, 12-14 Sept.,
12 2017, London, UK (pp. 338–345). London.

13 Richards, I.A., Byrne, B.W., & Houlsby, G.T., 2019. Monopile rotation under complex cyclic lateral loading in
14 sand. *Géotechnique*, Ahead of Print.

15 Richards, I.A., 2019. Monopile foundations under complex cyclic lateral loading, DPhil thesis, University of
16 Oxford.

17 Roy, A., Chow, C., O’Loughlin, C., Randolph, M., 2019. Effect of stress history and shallow embedment on
18 centrifuge cone penetration tests in sand. In Proceedings of the ASME 2019 39th International Conference on
19 *Ocean, Offshore and Arctic Engineering (OMAE2019)*. Glasgow, Scotland.

20 Rudolph, C., Bienen, B. & Grabe, J., 2014a. Effect of variation of the loading direction on the displacement
21 accumulation of large-diameter piles under cyclic lateral loading in sand. *Canadian Geotechnical Journal*,
22 51(10), 1196–1206.

23 Rudolph, C., Grabe, J. & Bienen, B., 2014b. Drift of piles subjected to cyclic lateral loading from a varying
24 direction: system vs. soil element behaviour. In Proceedings of ASME 2014 33rd International Conference on
25 *Ocean, Offshore and Arctic Engineering*. San Francisco, USA.

26 Schroeder, F. C., Merritt, A. S., Sørensen, K. W., Muir Wood, A., Thilsted, C. L., and Potts, D. M. (2015).
27 Predicting monopile behaviour for the Gode Wind offshore wind farm. Proceedings of the 3rd International
28 *Symposium on Frontiers in Offshore Geotechnics (ISFOG)*. Oslo, Norway, pp. 735–740.

- 1 Sørensen, S. P. H., Augustesen, A. H., Leth, C. T., Østergaard, M. U., and Møller, M. (2017). Consequences of
2 p-y curve selection for monopile design for offshore wind turbines. In *Proceedings of the 8th International*
3 *Conference on Offshore Site Investigation and Geotechnics (SUT)*. London, UK, pp. 1062–1069.
- 4 Tatsuoka, F., Sakamoto, S., Kawamura, T., Fukushima, S., 1986. Strength and deformation characteristics of
5 sand in plane strain compression at extremely low pressures. *Soils and Foundations*, 26(1), 65–84.
- 6 Truong, P., Lehane, B.M., Zania, V., Klinkvort, R.T., 2019. Empirical approach based on centrifuge testing for
7 cyclic deformations of laterally loaded piles in sand. *Géotechnique*, 69(2), 133–145.
- 8 White, J. R. F. (2020). A laboratory investigation into the behaviour of sand at low confining stresses.
9 Forthcoming DPhil thesis, University of Oxford.
- 10 Wind Europe. (2018). Offshore Wind in Europe: Key trends and statistics 2017. Available online:
11 [https://windeurope.org/wp-content/uploads/files/about-wind/statistics/WindEurope-Annual-Offshore-](https://windeurope.org/wp-content/uploads/files/about-wind/statistics/WindEurope-Annual-Offshore-Statistics-2017.pdf)
12 [Statistics-2017.pdf](https://windeurope.org/wp-content/uploads/files/about-wind/statistics/WindEurope-Annual-Offshore-Statistics-2017.pdf).